*29th EPS Conference on Plasma Phys. and Contr. Fusion Montreux, 17-21 June 2002 ECA Vol. **26B**, P-1.024 (2002)*

Integrated Predictive Transport Modelling of ELMy H-Mode JET Plasmas

J.S. Lönnroth[1], G. Corrigan[2], D. Heading[2], G. Huysmans[3], A. Loarte[4], V.V. Parail[2], G. Saibene[4], S. Sharapov[2], J. Spence[2] and contributors to the EFDA-JET work programme

[1]Association EURATOM-Tekes, Helsinki University of Technology, P.O. Box 2200, 02015 HUT, Finland; [2]EURATOM/UKAEA Fusion Association, Culham Science Centre, Abingdon, Oxon OX14 3DB, UK; [3]Association EURATOM-CEA, CEA Cadarache, DRFC, Bâtiment 513, 13108 Saint-Paul-Lez-Durance, France; [4]EFDA Close Support Unit, c/o MPI für Plasmaphysik, Boltzmannstrasse 2, 85748 Garching, Germany

1. Introduction

It is well-known that the edge plasma parameters influence plasma performance in many different ways. In the ELMy H-mode, which is considered a reference scenario for ITER and other burning plasma experiments, the link between edge and core is controlled by the edge transport barrier (ETB), a thin layer of improved transport characteristics. Conventionally, the plasma core and scrape-off layer have been treated separately in predictive modelling with the motivation that the physics is very different in these two regions. Moreover, in many studies modelling of the plasma has not included simulation of the ETB and the scrape-off layer. Instead, the values of the relevant plasma parameters on top of the ETB have been used as boundary conditions. However, both theory and experiments show that there is a strong link between the edge and the core, so that even a modest variation of the plasma parameters in one region can lead to a dramatic change in overall plasma performance. Therefore, integrated modelling of both core and edge is needed in order to obtain self-consistent results.

In this study, integrated predicted modelling of ELMy H-mode JET plasmas is performed using a suite of JET transport codes. Core modelling is done with the 1.5D transport code JETTO [1], whose output is linked to the MHD stability codes IDBALL, HELENA and MISHKA [2]. The edge transport code EDGE2D/NIMBUS [3] is used for 2D modelling of the scrape-off layer. Finally, both core and edge are modelled self-consistently using COCONUT, a coupling of EDGE2D and JETTO. The coupled runs also give self-consistent boundary conditions for the JETTO runs on which MHD stability analysis is performed.

2. Integrated predictive modelling

The sensitive dependence of plasma performance on the edge parameters is very well demonstrated in experiments with external gas fuelling in type I ELMy H-mode plasma [4]. It is known from experiments that plasma easily accommodates modest gas puffing, e.g. a neutral influx of $\Gamma = 3 \cdot 10^{22}$ s^{-1} in the case of JET. Higher levels of gas puffing can trigger a transition from type I to type III ELMs with a dramatic increase in the ELM frequency followed by a deterioration of plasma confinement. As will be shown, these experimental observations can be explained by predictive simulations.

An increase in the neutral gas puffing influences the scrape-off layer in the first place. Predictive modelling unravels a chain of causalities illustrated by Fig. 1. In Fig. 1, the profiles of a number of relevant plasma parameters have been plotted for two predictive simulations with different levels of gas puffing: $\Gamma = 0$ and $\Gamma = 4 \cdot 10^{22}$ s^{-1}. As shown in Fig. 1, an increase in the level of gas puffing leads to an increase in the edge density. Integrated modelling with COCONUT explains the sharp increase in edge density by showing that the neutral influx from the scrape-off layer through the separatrix is only a small fraction of the total neutral gas puffing. It can also be seen that both the ion and electron temperatures at the separatrix decrease, which is due to increasing

neo-classical losses. As a result of the increased collisionality at the edge, there is a significant decrease of the bootstrap current, also shown in Fig. 1. To a first approximation, the bootstrap current is inversely proportional to the collisionality. Hence, the edge current, which comprises of both bootstrap and Ohmic current, decreases significantly, as illustrated by Fig. 1. Magnetic shear, also plotted in Fig. 1, increases with decreasing edge current. Finally, magnetic shear controls MHD stability in general and $n = \infty$ ballooning stability in particular. In this way, external gas fuelling affects ballooning stability very sensitively. This is illustrated in Fig. 2, which shows how predictive modelling can explain the experimentally observed transition from type I to type III ELMs and change in ELM frequency: Increasing shear causes a transition from second to first $n = \infty$ ballooning stability.

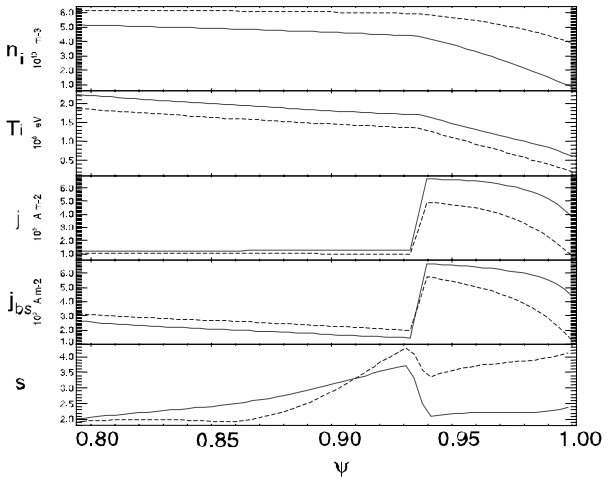

Figure 1. Ion density, ion temperature, bootstrap current, total current and magnetic shear in predictive simulations with two different levels of gas fuelling $\Gamma = 0$ (full line) and $\Gamma = 4 \cdot 10^{22}$ s^{-1} (dashed line).

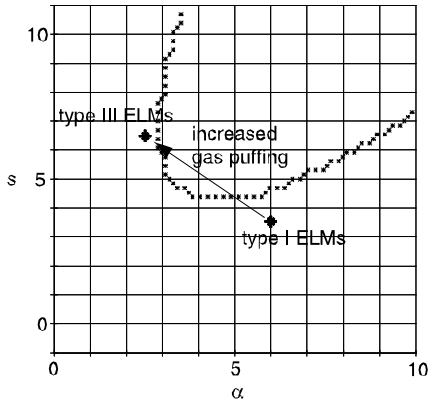

Figure 2. Experiments have shown that strong gas puffing can trigger a transition from type I to type III ELMs with a dramatic increase in the ELM frequency followed by a deterioration of plasma confinement. Predictive modelling explains this as a transition from second to first $n = \infty$ ballooning stability.

In this study, the high-triangularity ($\delta = 0.5$) ELMy H-mode JET discharge 53298 has been selected for the analysis. A scan in gas puffing has been performed with the integrated code COCONUT. Some results from the scan are summarized in Table 1. The results are self-consistent, because the whole core, the ETB and the scrape-off layer are modelled together. As discussed before, Table 1 shows that the edge density increases with the level of external gas fuelling, because the neutral influx from the scrape-off layer through the separatrix is much smaller than the total gas puffing. Also shown is that the edge temperature decreases for increasing edge density.

Table 1. Ion density and temperature at the separatrix as a function of the rate of gas puffing in a few COCONUT runs.

Puff rate	Ion density at separatrix	Ion temperature at separatrix	Neutral influx through separatrix
$2 \cdot 10^{22}$ s^{-1}	$2.95 \cdot 10^{19}$ m^{-3}	354 eV	$9.07 \cdot 10^{20}$ s^{-1}
$8 \cdot 10^{22}$ s^{-1}	$7.67 \cdot 10^{19}$ m^{-3}	193 eV	$5.62 \cdot 10^{20}$ s^{-1}
$1 \cdot 10^{23}$ s^{-1}	$8.39 \cdot 10^{19}$ m^{-3}	178 eV	$4.18 \cdot 10^{20}$ s^{-1}

The self-consistently calculated edge densities and temperatures in Table. 1 have been used as boundary conditions in stand-alone JETTO runs, on which ballooning stability analysis has been performed. The analysis shows that gas puffing indeed influences ballooning stability very sensitively. For a modest rate of gas puffing, the operational point in terms of normalized pressure gradient and magnetic shear can enter second ballooning stability for magnetic surfaces corresponding to the top the ETB. The modelling shows that by increasing the level of gas puffing one can trigger a transition from second to first ballooning stability accompanied by a transition from type I to type III ELMs.

3. MHD stability analysis

MHD stability analysis has been performed on JETTO runs with the boundary conditions obtained from self-consistent COCONUT runs. Three different levels of external gas fuelling have been considered: $\Gamma = 0$, $\Gamma = 4\cdot 10^{22}$ s^{-1} and $\Gamma = 1\cdot 10^{23}$ s^{-1}. Here, the corresponding JETTO runs will be referred to as Runs 1, 2 and 3. Table 1 shows the values of density and temperature at the separatrix used in each case. However, ELMs have not been modelled in these runs.

Table 2. The edge density and the edge temperature in three runs with different levels of external gas fuelling as calculated self-consistently by COCONUT.

	Puff rate Γ	Edge density n_0	Edge temperature T_0
Run 1	0	$5 \cdot 10^{18}$ m^{-3}	600 eV
Run 2	$4\cdot 10^{22}$ s^{-1}	$3.7 \cdot 10^{19}$ m^{-3}	200 eV
Run 3	$1.0\cdot 10^{23}$ s^{-1}	$8.0 \cdot 10^{19}$ m^{-3}	180 eV

Figures 3 and 4 illustrate the results of a comprehensive MHD stability analysis performed using MISHKA and HELENA for $\Gamma = 0$ and $\Gamma = 4\cdot 10^{22}$ s^{-1}. The mode number of the most unstable ballooning or peeling mode has been printed onto the figures wherever appropriate in a co-ordinate system with the normalized pressure gradient $\alpha = -2\mu_0 q^2/(B_0^2\varepsilon)\mathrm{d}p/\mathrm{d}\rho$ on the horizontal axis and magnetic shear s on the vertical one. Here, μ_0 is permeability of vacuum, q is the safety factor, B_0 is the magnetic field on the magnetic axis, ε is the inverse aspect ratio, p is the pressure and ρ is the toroidal flux co-ordinate. One can easily make out three distinct regions on the plot: a region with no instabilities, a region in which the low n kink instability is dominant and a region in which the high n ballooning instability dominates. The $n = \infty$ ballooning unstable region has also been marked in the figures. In addition, the plots show the location of the operational point for a number of different magnetic surfaces, so that the trajectory of the operational point can be inferred.

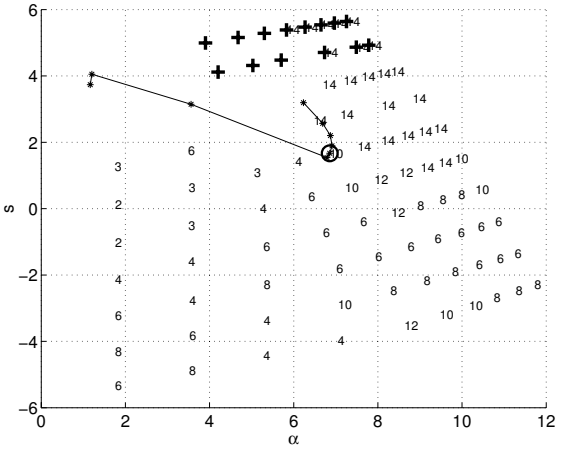

Figure 3. MHD stability diagram for Run 1. The numbers indicate the mode number of the most unstable mode. The $n = \infty$ ballooning unstable region has been marked with crosses. The operational point has been plotted for ρ = 0.920, 0.929, 0.939, 0.948, 0.953, 0.962, 0.972, 0.981 and 0.990. The location of the top of the ETB has been marked with a circle.

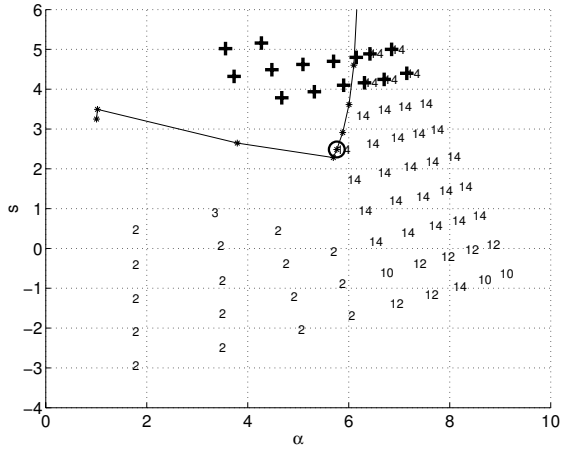

Figure 4. MHD stability diagram for Run 2. The symbols in the figure are to be interpreted as in Fig. 2. The operational point has been plotted for ρ = 0.919, 0.929, 0.939, 0.947, 0.952, 0.961, 0.971 and 0.980.

Figure 3 illustrates the fact that Run 1 with zero gas puffing is very kink unstable, because the edge current is high due to the low edge density. However, there is still a gap with access to second $n = \infty$ ballooning stability, but it closes when $s < 2$. For increasing ρ, the operational point moves from the first stability region to the second stability region without touching the $n = \infty$ ballooning stability limit. The system remains in the second stability region for ρ values corre-

sponding to the ETB. The maximum operational α is limited by a region of finite *n* ballooning instability.

In Fig. 4 corresponding to Run 2 with the intermediate level of gas puffing, the system is more kink stable, because the edge current is significantly smaller for the higher level of gas fuelling. Access to second stability opens readily, since the kink instability is suppressed. Again, the maximum operational α, in this case $\alpha \approx 6$, is defined by a region of $n = 14$ ballooning instability. For ρ corresponding to the top of the ETB, the system is in the second stability region. Closer to the edge, however, the system is $n = \infty$ ballooning unstable, because shear increases dramatically there.

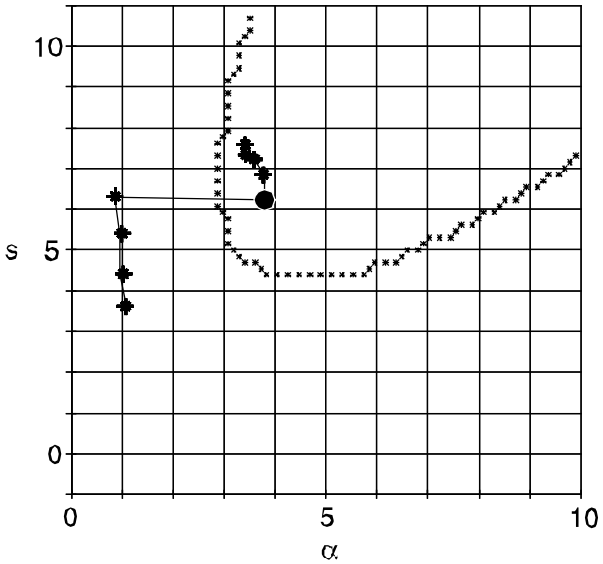

Figure 2. n = ∞ ballooning stability diagram for Run 3 calculated with IDBALL. The boundary of the unstable region is shown. The operational point has been plotted for ψ = 0.910, 0.920, 0.930, 0.940, 0.950, 0.960, 0.970 and 0.980. The largest point corresponds to the top of the ETB.

Figure 5 shows an $n = \infty$ ballooning stability diagram calculated by IDBALL for Run 3 with the strongest level of gas fuelling. In this case, the edge current is vanishingly small, whereby magnetic shear is strong and access to second stability is closed. The operational point moves from first stability to the unstable region as ρ increases.

From the comparison between Figs. 3, 4 and 5, it can be inferred that by increasing the level of gas puffing one can eventually trigger a transition from second to first $n = \infty$ ballooning stability. Modelling shows that as the transition occurs, the ELM frequency increases dramatically. The reason for this is that the inherent critical pressure gradient of the system decreases from typically about $\alpha \approx 6$ defined by the boundary of the finite *n* ballooning unstable region in the case of second stability to typically about $\alpha \approx 3$ defined by the first stability limit, as illustrated by Fig. 1. The change is accompanied by a transition from type I to type III ELMs.

4. Summary and discussion

In this work, integrated predictive modelling of ELMy H-mode JET plasmas has been performed using the coupled code COCONUT. It has been shown that external gas fuelling can very sensitively affect ballooning and peeling / kink stability via its influence on edge density, collisionality, bootstrap current and shear. MHD stability analysis has been performed on JETTO runs using boundary conditions calculated self-consistently by COCONUT. It has been shown that the plasma can gain access to second $n = \infty$ ballooning stability in many cases, such as with moderate gas puffing. The transition to second stability can be controlled either by the peeling and the finite *n* ballooning mode or by $n = \infty$ ballooning stability. It has also been shown that strong gas puffing can trigger a transition from second to first stability.

[1] G. Cennachi, A. Taroni, JET-IR(88)03 (1988).
[2] A.B. Mikhailovskii *et al*., Plasma Phys. Rep. **23** 844 (1997).
[3] R. Simonini *et al*., Contrib. Plasma Phys. **34** 368 (1994).
[4] G. Saibene *et al*., Proc. 28th EPS Conference on Controlled Fusion and Plasma Physics, Madeira, 18-22 June 2001.